



Impedance spectroscopic analysis of high-performance dye sensitized solar cells based on nano-clay electrolytes



Victoria González Pedro^{a,b,*}, Hideki Sakurai^c, Mitsuru Tomita^c, Bruno Ieiri Ito^c,
Francisco Fabregat Santiago^a, Satoshi Uchida^{d,*}, Hiroshi Segawa^{c,*}

^a Institute of Advanced Materials (INAM), Universitat Jaume I, 12071 Castelló, Spain

^b Instituto interuniversitario de Reconocimiento Molecular y Desarrollo Tecnológico (IDM), Departamento de Química, Universitat Politècnica de València, Camino de Vera s/n, E46071 Valencia, Spain

^c Research Center for Advanced Science and Technology, The University of Tokyo, Komaba 4-6-1, Meguro-ku, Tokyo 153-8904, Japan

^d Komaba Organization for Educational Excellence, The University of Tokyo, Komaba 3-8-1, Meguro-ku, Tokyo 153-8902, Japan

ARTICLE INFO

Article history:

Received 29 October 2015

Received in revised form 9 February 2016

Accepted 4 March 2016

Available online 6 March 2016

Keywords:

sensitized solar cells
nano-clay electrolytes
impedance
Spectroscopy

ABSTRACT

In this work we present quasi-solid state dye-sensitized solar cells obtained employing artificial hydrotalcite nano-clay as electrolyte additive, with a greatly improved photo-energy conversion efficiency of up to 10.9% with respect to the 9.6% obtained for liquid electrolyte ruthenium based reference cell. Through impedance spectroscopy, we have evaluated quantitatively the effects of shifts in the conduction band energy level and variations of electron recombination rates over the photovoltage. We demonstrated that the origin of these changes could be ascribed to the chemical effects induced by the fluctuation of ionic species inside the pores of TiO₂ in the presence of nano-clay. These results highlight the dual functionality of clay electrolyte that enables the fabrication of stable solar devices under irradiation tests over 1000 h, and pushes up the photo-energy conversion efficiency up to a record values.

© 2016 Elsevier Ltd. All rights reserved.

1. Introduction

Dye-sensitized solar cells (DSCs) have generally attracted much attention as they offer the possibility of getting extremely inexpensive and efficient solar energy conversion. [1–3] However, the presence of liquid electrolytes in such modules may result in some practical limitations, being long-term stability due to the leakage of the liquid electrolyte one of the most relevant.

To overcome the drawbacks of liquid electrolytes several studies have proposed the use of solid hole transporting materials, such as p-type semiconductors [4–6], organic materials [7–9] and solvent-free polymer electrolytes incorporating triiodide/iodide as a redox couple [10–13]. Nevertheless, these materials stumble with the lower ionic mobility and poor pore-filling ability of solid electrolytes. [14] In this context, the quasi-solid electrolytes, including ionic liquids and gel electrolytes, meet the merits of both liquid and solid ones. [15–18] A common approach for gelating is mixing standard liquids electrolytes with inorganic compounds

generating robust and stable hybrid nanocomposites. Grätzel et al. demonstrated for the first time the potential of these gel electrolytes by the addition of SiO₂ nanoparticles as solidifying agent in a DSCs [19]. This work triggered the interest to explore the use of inorganic materials as gelators [13,20–22]. In addition, nano-clay based electrolytes have some unique advantages such as its abundance in nature, high chemical stability and it is low toxicity [23,24].

Reviewing the literature, it could be observed that a wide variety of nano-clay electrolyte have been proposed, such as saponite [23,25] and laponite based nanocomposites, and polymer-gel electrolytes containing montmorillonite or tin oxide [13,26]. However, according to these reports, the cells performance are still low because they are mostly using naturally occurring minerals, whose properties are often associated with the source and extraction methods. This issue can be solved by the design of artificial nano-clay, as the recently reported synthetic nanocomposites based on hydrotalcite structure that have achieved efficiencies over 10% [24,27].

Based on the state-of-the-art progress, the benefits of clay are not just solidifying the electrolyte leading to more stable devices, they also contribute to enhance the cell performance. Several mechanisms have been proposed to explain the role of the clay. On

* Corresponding author.

E-mail addresses: vicgonpe@upv.es (V. González Pedro),
uchida@rcast.u-tokyo.ac.jp (S. Uchida), csegawa@mail.ecc.u-tokyo.ac.jp
(H. Segawa).

the one side, physical effects such as, enhanced light scattering or differences in ionic conductivity due to the decrease of polymeric matrix crystallinity explain part of the performance improvements achieved. [23,28] On the other side, some benefits could be ascribed to the Lewis acidity-basicity of the inorganic particles, or the variation of dissolved species in the electrolyte, that induces changes in the photo-energy conversion efficiency, PCE. [13,24] Nevertheless, the chemical effects induced by nano-clay additives on the charge transfer mechanisms and recombination losses have not yet been elucidated in detail.

In this work we will deepen in the fundamental understanding of electron transfer mechanisms and the relationship between the recombination losses and photovoltage, E_{oc} , for nano-clay based quasi solid state DSCs. With the aid of impedance spectroscopy (IS) we have evaluated the effects of gel electrolyte over charge recombination in TiO_2 . This analysis will allow separating the contribution of TiO_2 CB shifts and recombination rate variations in the experimental photovoltage. In addition, the procedure proposed may be considered a good route to focus on the optimization of these types of electrolytes towards the development of a new generation of hybrid nanocomposites.

Finally, we have boosted solar conversion efficiency by adding Zr^{4+} cations to the nanoclay composition. The inclusion of zirconia (IV) produces solar conversion efficiencies of 10.9%, which is among the best efficiencies reported in the literature for ruthenium based DSCs.

2. Experimental section

Preparation of the nano-clay electrolyte. All chemicals were of reagent grade and used without further purification. The hydrotalcite (HT) nanoparticles were synthesized in the laboratory using the co-precipitation method as follows [29,30]: a solution containing 0.29 M of $\text{Mg}(\text{NO}_3)_2 \cdot 6\text{H}_2\text{O}$ and 0.11 M of $\text{Al}(\text{NO}_3)_3 \cdot 9\text{H}_2\text{O}$ (Mg:Al proportion of 3:1, Wako Pure Chemicals Industries, Ltd.) was mixed up with stirring. The basic solution containing 1.5 M of NaOH and 1.0 M of Na_2CO_3 (Wako Pure Chemicals Industries, Ltd.) were added dropwise to form the hydrolyzed precipitate. The reaction condition was maintained at pH 12 and 80 °C for 48 h. The obtained suspension was centrifuged (10,000 rpm, 10 min) and washed with deionized water several times in order to eliminate the reagents and impurities. The product was then dried using a freeze drier for 8 hours. The final powder was crushed with a pistil and a mortar and filtered by sieves with openings of 20 μm . A very fine and regular-sized powder was finally obtained. No were not remaining nitrate ions in the products, what was confirmed by ionic chromatograph Ion chromatography (PIA-1000, Shimadzu Corp.).

The electrolyte was based on 0.1 M of lithium iodide (Sigma-Aldrich), 0.025 M of iodine (Kanto Chemical Co., Inc.), 0.6 M of 1,2-dimethyl-3-propylimidazolium iodide (DMPII, Shikoku Chemicals

Co.), 0.5 M of 4-*tert*-butylpyridine (TBP, Wako Pure Chemicals Industries, Ltd.) in dehydrated acetonitrile. The HT was added to the electrolyte in different concentrations and after that it was ultra-sonicated for dispersion.

Fabrication of the DSCs. The TiO_2 photoanode was prepared as described below. A thin layer of TiO_2 (Ti Nanoxide, Solaronix SA) was screen printed on a FTO conducting glass (F:SnO_2 , 10 Ω/cm^2 , Nippon Sheet Glass Co. Ltd.) using an Automatic alignment screen printer (LS-150TVA, Newlong Seimitsu Kogyo Co. Ltd.) for guaranteeing the repeatability. Then, it was sintered at 500 °C for 30 min. The sintered TiO_2 was immersed in a 50 mM of TiCl_4 aqueous solution for 30 min at 70 °C and then sintered again at 500 °C for 30 min. The film thickness of the final film was around 18 μm . The TiO_2 film was then immersed into an N719 dye solution of 0.3 mM concentration (Solaronix SA – $[(\text{C}_4\text{H}_9)_4\text{N}]_2[\text{Ru}(\text{II})\text{L}_2(\text{NCS})_2]$, where L=2,2'-bipyridyl-4,4'-dicarboxylic acid) in a solvent mixture of *tert*-butanol and acetonitrile (v:v=1:1) for 20 hours at 30 °C in the dark. In the similar manner Z907 (Solaronix SA–cis-di(thiocyanato)-(2,2'-bipyridyl-4,4'-dicarboxylic acid)-(Ru(II)-(4,4'-dinonyl-2,2'-bipyridyl))) was used for high durability test.

A platinum loaded ITO counter electrode and a 30 μm gap spacer sheet (Du Pont Mitsui Polychemicals Co., Ltd.) were used to construct the device. For the DSC assembly, two drops of the electrolyte were dropped over the TiO_2 electrode and later, it was sandwiched by using the counter electrode with the spacer in the middle.

Structural characterization. The nano-clay image was obtained using a field-emission scanning electron microscope, FE-SEM (JSM-7500F, JEOL Ltd.) with a semi-in-lens and equipped with a Gentle Beam to deliver high-resolution at acceleration voltage 0.5 kV.

Photoelectrochemical characterization. The J-E curves were measured using a mask (0.16 cm^2) by Potentiostat (HSV-110, Hokuto Denko) with class AAA Solar simulator (YSS-80 Yamashita Denso Corp.) to give 100 $\text{mW}\cdot\text{cm}^{-2}$ irradiance with the global spectrum distribution (AM1.5G). The light intensity was calibrated using a certified Si solar cell.

The IPCE (Incident photon-to-current efficiency) measurement was performed with Spectral response measurement system (CEP-2000, Bunko-Keiki Co. Ltd.) by giving monochromatic light from 300 to 800 nm.

Impedance spectroscopy measurements were carried out using Impedance gain-phase analyzer (SI 1260, Solartron) under an irradiation of 1 sun (AM 1.5 G conditions), different bias potentials, that ranged from zero to open-circuit voltage, and frequencies between 1 MHz and 0.1 Hz. Impedance measurements were performed using a controlled temperature unit Compact ultra low temperature chamber (MC-711, ESPEC).

Quantitative analysis of ionic species in the electrolyte. The evolution of ionic species in the electrolyte upon nanoclay addition was evaluated by Atomic Absorption Spectrometry (AAS) for

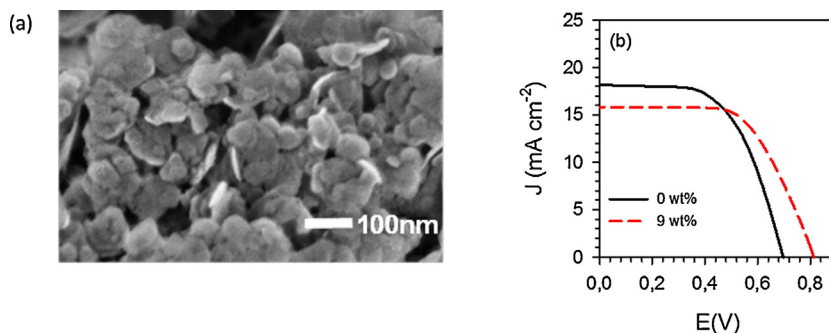


Fig. 1. Field emission scanning electron micrograph of nano-clay synthesized at 80 °C for 48 h. (b) J-E curves of liquid and quasi solid DSCs.

lithium cations and UV–vis spectroscopy for iodide species. To estimate the adsorption ability of lithium, solutions of 2 mL of LiI (0.1 M) in acetonitrile with different nano-clay weight percentages (0–12 wt%) were prepared. Then, they were filtered by 0.2 µm pore size membrane. The solution was heated to evaporate the acetonitrile and diluted in pure water for the measurement. Lithium concentration was determined by Atomic Absorption Spectrometry (Shimadzu AA-7000) using $\lambda = 670.784$ nm as analytical line for lithium.

Iodide and triiodide free species were determined from the filtered electrolyte solutions (0.7 M LiI and 0.025 M I₂ in acetonitrile) by UV–vis spectroscopy (Agilent 8453) at 250 nm for iodide and 290 nm for triiodide. The adsorbed amount of iodide and triiodide species on hydrotalcite was quantified by comparison with the free nano-clay solution.

3. Results and discussion

Photovoltaic performance of DSCs. The representative FE-SEM image of the synthesized nano-clay Mg_{0.75}Al_{0.25}-(OH)₂(CO₃)_{0.125}·0.25H₂O is shown in Fig. 1a. An unformed hexagonal plate like particles with diameter about 80 nm was observed.

Fig. 1 b shows the current voltage (J-E) curves recorded for the DSCs cells using liquid and 9 wt% nano-clay electrolyte. The resulting photovoltaic parameters are summarized in Table 1. Note that the quasi-solid electrolyte device presents higher open-circuit voltage (E_{oc}) in comparison with the reference solar cell. Previous studies reported that the improvement in E_{oc} using nano-clay electrolytes has its origin in a shift of the conduction band position which could be attributed to the higher basicity of the electrolyte [24] yielding to a drop of positive species in contact with TiO₂ surface. In contrast, the reference solar cell presents larger photocurrent density, 18.1 mA·cm⁻². Lower J_{sc} could be associated with the upwards shift in the conduction band position in presence of the nano-clay electrolyte that hinders the electron injection.

Regarding the stability, the time dependent efficiency under illumination for both electrolytes is depicted in Fig. S1 (Supporting Information). The nano-clay cell presents a stable performance after initial rise exceeding 1000 hours in contrast to the slow decay in liquid electrolyte after 400 hours of operation. Therefore, it is noteworthy the dual functionality of the clay additive that solidifies the electrolyte without sacrificing the solar cell performance.

Ionic transport in the quasi solid state electrolyte and charge transfer resistance in the Pt-FTO/Electrolyte. To scrutinize the interfacial properties between Pt counter electrode and the electrolyte, symmetric Pt-Pt cells were assembled and characterized by means of cyclic voltametry and impedance spectroscopy. The cyclic voltametries are depicted in Fig. 2a. Both curves exhibit similar slope, and thus, it is expected that both electrolytes present similar resistance values. Taking the limiting current densities values the diffusion coefficients can be determined according to the following equation

$$D = \frac{d}{2nFc} J_{lim} \quad (1)$$

Table 1
Photovoltaic performances of the liquid and quasi solid state DSCs.

Nano-clay (wt %)	J_{sc} (mA·cm ⁻²)	E_{oc} (mV)	FF	η (%)	$D_{I_3^-}$ (cm ² ·s ⁻¹)
0	18.1	697	0.58	7.32	$5.6 \cdot 10^{-6}$
9	15.8	813	0.61	7.84	$4.9 \cdot 10^{-6}$

where $n = 2$ is the electron transferred in the reduction from I₃⁻ to I⁻, c is the bulk concentration of triiodide species, d the distance between electrodes and F the faraday constant. The diffusion coefficients, $4.9 \cdot 10^{-6}$ cm²·s⁻¹ and $5.6 \cdot 10^{-6}$ cm²·s⁻¹ for the gel electrolyte and the reference, respectively, are in good correlation with previous reported values. [13,24] The increased viscosity of the gel electrolyte reduces the mobility of ions and consequently, diffusion coefficient of I₃⁻ is slightly smaller than in pure liquid. However, saturation current extracted in Fig. 2a is still double than the maximum current obtained by a complete cell. Therefore, we can conclude that the effect on current of operating DSC is minimal. Further analysis by impedance spectroscopy provides information of charge accumulation, transport and resistance phenomena in the counterelectrodes. The impedance spectra were fitted according to the equivalent circuit shown in the inset of Fig. 2c. Where R_s represents the resistance associated to transport in FTO, bulk of electrolyte and electrical connections, C_{dl} the double layer capacitance at the interface between platinized FTO electrode and electrolyte, and R_{ct} the charge transfer resistance at the same interface. The factor 2 is associated to the presence of two Pt electrodes. Finally, Z_d is the diffusion impedance given by

$$Z_d = R_d \frac{\tanh(j\omega/\omega_d)^{1/2}}{(j\omega/\omega_d)^{1/2}} \quad (2)$$

where R_d is the diffusion resistance, $j = \sqrt{-1}$, ω is the angular frequency of the measurement and $\omega_d = D/L^2$ the diffusion frequency, with D the diffusion coefficient and L the thickness of the diffusion boundary layer.

Charge transfer resistance at the Pt-FTO/electrolyte interface and diffusion resistance at different applied voltages are plot in Fig. 2b and 2c, respectively. The impedance data indicates non-significant differences within both electrolytes. Therefore, as the transport and electrocatalytic properties of the electrolyte and counter electrode remain unaltered upon clay addition we can conclude that these parameters are not the origin of the changes observed in solar cell performance. In addition, the diffusion boundary layer at different applied bias, which was extracted from the impedance and is depicted in Fig. S3c of SI, are 25 µm and 24 µm, respectively. These values correlate well with previously reported for iodine liquid electrolytes. [31]

Analysis of E_{oc} in quasi-solid electrolyte solar cells. For further insight of the effects of nano-clay electrolyte in photovoltaic parameters we again use IS technique. Detailed information about the interpretation of the parameters obtained through IS analysis and the cell performance is reported in the literature. Here we will focus in the most relevant aspects needed to understand our samples [32–34]. Simplified equivalent circuit used to fit IS of complete solar cells under illumination is plot in Fig. 3a. Note that in our samples contribution from transport resistance in TiO₂ was irrelevant, so we avoided to use the more complex transmission line model. [32] In this model, C_{film} represents the capacitance of the film. At potentials higher than 0.4 V for sample without clay and 0.6 V for sample with clay, chemical capacitance of TiO₂ nanoparticles dominate and film capacitance follows

$$C_{film} = C_0 \exp \left[\alpha \frac{qE_F}{k_B T} \right] \quad (3)$$

with q the electron charge, k_B Boltzmann's constant, T the temperature, E_F the potential in the TiO₂ film, α a parameter associated to the distribution of sub-bandgap states in the TiO₂ and C_0

$$C_0 = \frac{\alpha q^2 N_L}{k_B T} \exp \left[\alpha \frac{E_{redox} - E_c}{k_B T} \right] \quad (4)$$

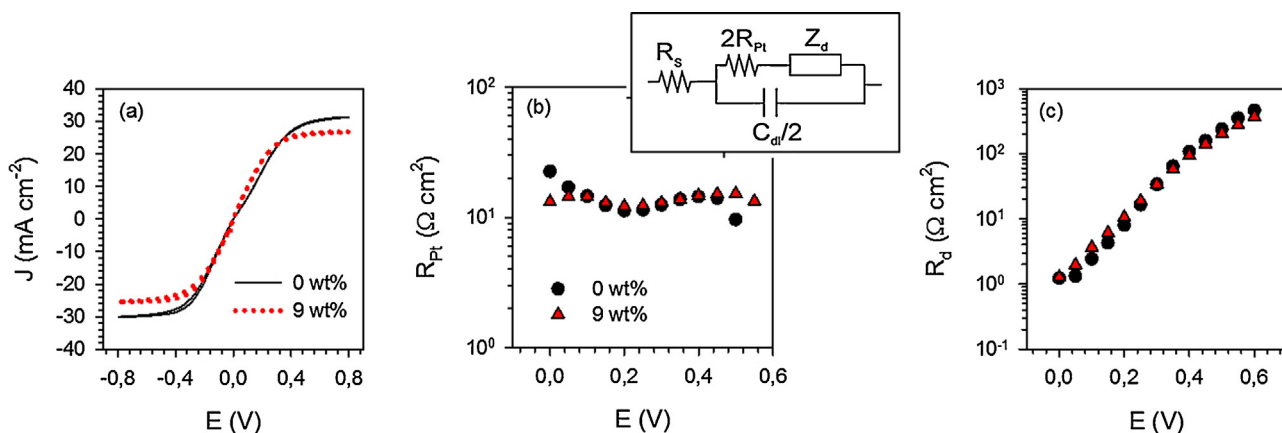


Fig. 2. (a) Cyclic voltammogram of standard (black line) and nano-clay gellified (red line) electrolytes. (b) Pt/Electrolyte charge transfer resistance and (c) electrolyte diffusion resistance at different applied bias. The resistances values were extracted from the impedance analysis of symmetric sandwich devices, Pt/Electrolyte/Pt, testing reference and $Mg_{0.75}Al_{0.25}(OH)_2(CO_3)_{0.125} \cdot 0.25H_2O$ nano-clay electrolyte (9 wt%). The IS data was fitted according to the circuit depicted in the inset.

a constant that depends on the relative position of conduction band (E_c) respect to the redox energy level (E_{redox}), and the total number of states below de conduction band (N_L).

R_{rec} is the recombination resistance that may be written as

$$R_{rec} = \left(\frac{dJ_{rec}}{dV_F} \right)^{-1} \approx R_0 \exp \left[-\beta \frac{qE_F}{k_B T} \right] \quad (5)$$

where J_{rec} is the current produced by recombination, β is a coefficient associated to the nonlinear recombination and R_0 is a parameter associated to the rate constant of recombination [35]. The chemical capacitance and recombination resistance obtained from the fitting of the Nyquist plots of the impedance spectra are shown in Figs. 3 and 4. These values have been represented after subtracting the effect of the series resistance on the voltage, $E_F = E_{app} - E_{series}$, according to procedures described elsewhere [35] with E_{app} the applied voltage and E_{series} the voltage drop at the total series resistance (here $R_{series} = R_s + R_{Pt} + R_d$).

In Fig. 3b it could be appreciated that the film capacitance extracted from the experimental data presents different behavior

depending on the voltage range. At low voltages, the capacitance associated to FTO substrate dominates film capacitance. At mid and high applied bias, the chemical capacitance of TiO_2 dominates C_{film} , showing its characteristic exponential dependence with voltage. The plateau region at very high voltage could be associated to chemical capacitance reaching values close to the surface Helmholtz capacitance of the TiO_2 /electrolyte interface or also to a change in the distribution of localized states at energies close to the conduction band. The alpha parameter, extracted from the slope at mid ($\alpha = 0.6$) and high ($\alpha = 0.1$) voltages, presents very close values for both devices, therefore we can conclude that the shape of the trap distribution in the TiO_2 does not change upon addition of clay. Taking into account that both electrodes have the same geometrical dimensions, and assuming that the number of traps in the DSC does not change, the shift observed in the capacitance is equivalent to a shift in the conduction band position. Therefore, the conduction band is shifted upwards by an amount $\Delta E_c/q = +175$ mV when the clay is added (Table 2). As the nano-clay size is too large (average diameter ~ 80 nm) to penetrate TiO_2 nanoporous matrix, the origin of this shift may only be associated

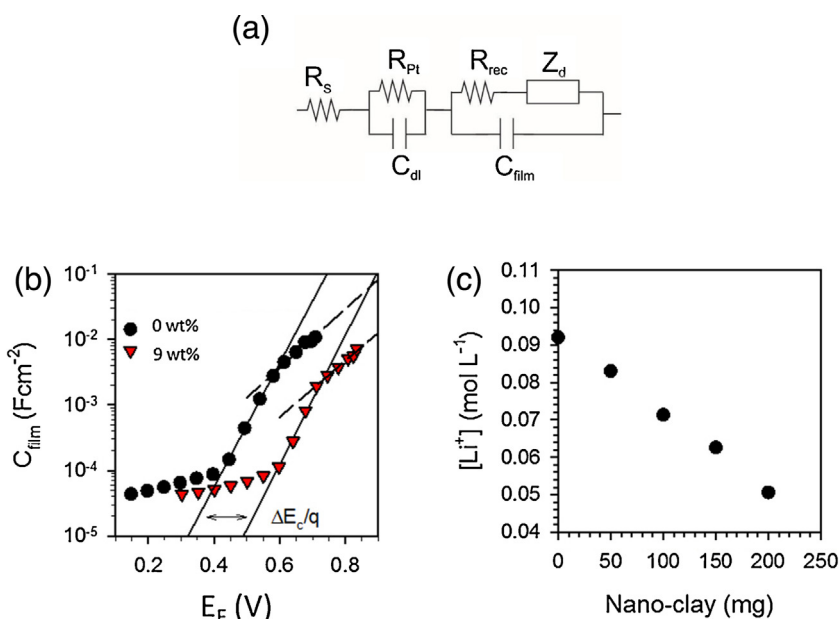


Fig. 3. (a) Equivalent circuit of DSC with and without nano-clay (b) Chemical capacitance as a function of fermi level voltage (removing the effect of series resistance), E_F , of reference and quasi solid DSC. (c) Evolution of Li^+ species in the electrolyte with different nano-clay weight.

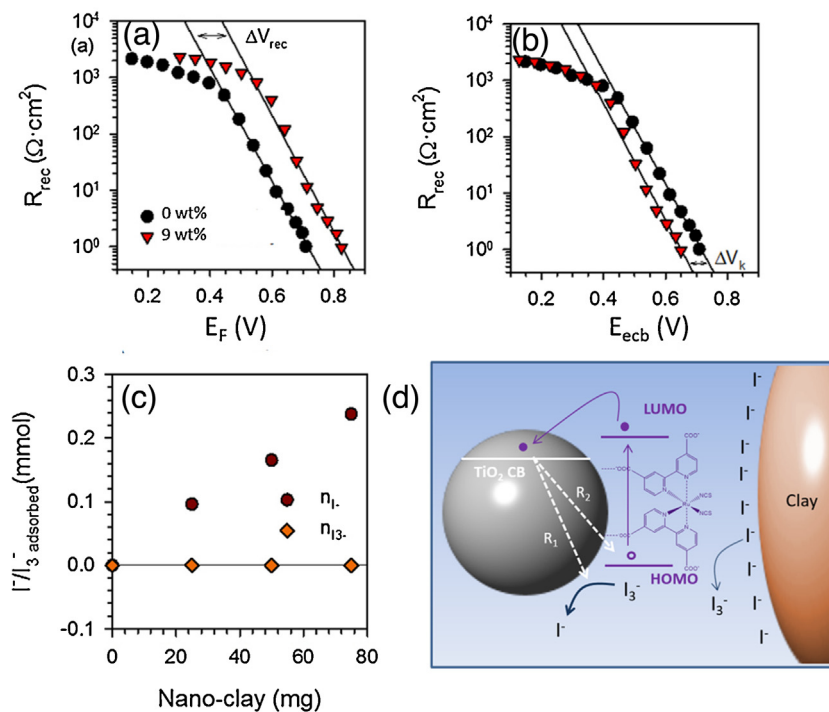


Fig. 4. Behavior of recombination resistance obtained by IS for liquid and gel electrolyte as function of (a) fermi voltage (subtracting the elect of series resistance), E_F , and (b) equivalent conduction band, E_{ecb} , where the displacement of the TiO_2 CB has been removed. (c) Evolution of the iodine and tri-iodine species adsorbed in the nano-clay. (d) Schematic diagram of the recombination losses in the photoanode/electrolyte interface.

with the variations of dissolved species in the electrolyte. In this respect, it is well known that alkaline cations dissolved in the electrolyte can be adsorbed in the surface of nano-clay leading to a downward shift of the conduction band position. This effect is attributed to higher basicity of the electrolyte and a smaller interaction of cation species on the surface of TiO_2 [36]. To confirm this hypothesis we quantify the adsorption of Li^+ species on nano-clay by means of conventional chemical analysis. In Fig. 3c is depicted the concentration of lithium species remaining in the electrolyte for different nano-clay weights. Paying attention to the graph the lithium species adsorb in the clay nanoparticles producing a drop of free cations inside the pores of TiO_2 . According to this data, the upward shift of the capacitance observed in Fig. 3b, is attributed to a reduction of Li^+ species in the presence of nano-clay. This fact is in good agreement with previous studies. [24] The recombination resistance of the quasi solid state solar cell, Fig. 4a, presents also an upward shift with potential in the gel electrolyte devices, yielding to lower recombination rates and thus, higher experimental photovoltage. Note that at low potentials recombination resistance presents a plateau region which is associated to direct transfer from FTO substrate to electrolyte. We focus our attention in the fast decaying resistance at mid and high potentials associated to electron losses from TiO_2 nanoparticles. It should be highlighted that the voltage shift $\Delta E_{rec} = +115$ mV matches very well with the experimental data $\Delta E_{oc} = +116$ mV, and the

remaining 1 mV is caused by the difference in photocurrent for both samples. Part of this displacement may attribute to the change of TiO_2 E_c mentioned above. However $\Delta E_c/q$ exceeds by 60 mV the change in ΔE_{rec} indicating that recombination kinetics is accelerated when clay is added to electrolyte (Table 2).

To estimate the E_{oc} changes associated with the differences in recombination kinetics, we compare R_{rec} at a similar TiO_2 electron concentration, for which we calculate the voltage at equivalent conduction band position following relation[35]

$$E_{ecb} = E_F - \Delta E_c/q \quad (6)$$

And with this representation we find that upon voltage shift, $\Delta E_k = -60$ mV, indicating higher recombination rates upon nano-clay addition. There are two paths that may modify recombination kinetics: (i) Changes in direct recombination of electrons in TiO_2 with I_3^- anions in the electrolyte near TiO_2 surface and (ii) Changes in back electron transfer from electrons injected to TiO_2 to unregenerated dye cations. (Scheme in Fig. 4d). To unravel the origin of the different recombination kinetics, the amount of I^- and I_3^- species in the electrolyte was quantified and is depicted in Fig. 4c. The iodide and triiodide concentration was determined by UV-vis spectroscopy at 250 nm for $[\text{I}^-]$ and 290 nm for $[\text{I}_3^-]$. The direct recombination with I_3^- species in the electrolyte can be discarded attending to the following considerations: i) The amount of electrons in TiO_2 CB band has been leveled (Fig. 4b). ii) The

Table 2

Parameters extracted from IS analysis: R_s , series resistance of the cell; β and R_0 charge transfer coefficients for recombination of electron, extracted from the fitting of R_{rec} to Eq. (5); α the exponential electron trap distribution parameter extracted from the fitting of C_{film} to Eq. (3); $\Delta E_c/q$, is the energy shift needed to compare all the cells at the same CB level obtained after displacing the capacitances; ΔE_k is the voltage difference in R_{rec} due to differences in recombination rates; ΔE_{rec} is the sum of $\Delta E_c/q$ and ΔE_k ; and ΔE_{oc} is the experimental photovoltage drop within liquid and quasi solid state DSCs.

Nano-clay (wt%)	R_s ($\Omega \cdot \text{cm}^2$)	R_0 ($\Omega \cdot \text{cm}^2$)	β_{midv}	C_0 (F/cm ²)	α_{midv}	α_{niv}	$\Delta E_c/q$ (mV)	ΔE_k (mV)	ΔE_{rec} (mV)	ΔE_{oc} (mV)
0	1.99	$1.53 \cdot 10^7$	0.59	$9.16 \cdot 10^{-9}$	0.56	0.11	–	–	–	–
9	1.43	$3.43 \cdot 10^8$	0.61	$1.46 \cdot 10^{-10}$	0.58	0.12	+175	–60	+115	+116

Table 3

Photovoltaic performances of DSC with clay ($\text{Mg}_{0.75}\text{Zr}_{0.175}\text{Al}_{0.075}(\text{OH})_2(\text{CO}_3)_{0.213} \cdot 0.25\text{H}_2\text{O}$, 9 wt%) in the electrolyte.

Clay (wt%)	E_{oc} (mV)	J_{sc} ($\text{mA}\cdot\text{cm}^{-2}$)	FF	η (%)
0	726	20.3	0.65	9.6
9	799	18.9	0.72	10.9

recombination kinetic constant of electrons with I_3^- anions is expected to remain constant as addition of clay is not in direct contact with TiO_2 surface except at the outer part of the film. iii) The concentration of tri-iodine species in the electrolyte is independent of clay concentration.

In contrast, the reduction of free I^- in the electrolyte with the increasing concentration of clay has as a consequence the reduction in the efficiency for dye regeneration. This fact activates recombination from the TiO_2 surface to the dye molecules [37] and produces a decrease in photocurrent generated.

In light of these results the chemical effects induced by the gel electrolyte produce a shift in conduction band, while keeping nearly constant the distribution of electronic states below the TiO_2 conduction band. We also find that the kinetics of charge transfer is also changed, inducing measurable effects in the photopotential, ΔE_k . It should be remarked that the experimental E_{oc} can be expressed as the sum of ΔE_k and $\Delta E_c/q$ which represents the main contributions to photovoltage, while contribution from the difference in photocurrent, ΔE_j , only contributes with 1 mV.

Analysis of J_{sc} and FF in quasi solid state electrolytes. The presence of nano-clay in the electrolyte induces a drop in the short circuit photocurrent values. As evidenced previously in Fig. 2 the bulk diffusion of the electrolyte and the diffusion resistances present very similar values both before and after nano-clay addition, therefore we can rule out ionic transport limitation in the electrolyte. The origin of this lower photocurrents may be attributed to: (i) the upward shift in the conduction band that reduces electron injection yield and (ii) the drop of I^- species in the electrolyte due to its absorption in the clay surface, that hinders dye regeneration rates and thus electron injection.

On the other hand, the Fill Factor in the cell increases with the addition of clay. This is associated mainly to the lower current flowing through the sample with clay that reduces the ohmic drop at resistances contributing in series (i.e. R_s and R_d). A small contribution to increase FF is the reduction of R_s in the cell with clay.

Finally, in latter studies the final solar cell performance has enhanced to 9.2% in pure liquid DSCs and 9.8% in gel electrolyte with clay ($\text{Mg}_{0.72}\text{Al}_{0.28}(\text{OH})_2(\text{CO}_3)_{0.31} \cdot 0.25\text{H}_2\text{O}$, 9 wt%) as shown in Fig. S5 and Table S1 in SI. In addition, further optimization was carried out adding small amounts of Zr^{4+} to the nano-clay composition. Optimized results, shown in Fig. S6 and Table 3, were obtained for nano-clay composition $\text{Mg}_{0.75}\text{Zr}_{0.175}\text{Al}_{0.075}(\text{OH})_2(\text{CO}_3)_{0.213} \cdot 0.25\text{H}_2\text{O}$. It is remarkably the improvement in solar cell performance from 9.6% to 10.9% when zirconia is added to the nano-clay recipe. This improvement was mostly originated by the enhancement of E_{oc} and Fill Factor, but despite the improvement in cell performance the general trend is the same as the Zr free nano-clay, and thus all the conclusions extracted from the impedance spectroscopy analysis can also be applied in these devices.

4. Conclusions

The quasi-solid state solar cell based on the employment of $\text{Mg}_{1-x}\text{Al}_x(\text{OH})_2(\text{CO}_3)_n \cdot m\text{H}_2\text{O}$ as solidifying agent has reported efficiencies of up to 9.8% (nano-clay without Zr) and 10.9% (nano-clay with Zr^{4+}). To our best knowledge this is the highest

efficiency reported for ruthenium based quasi solid state solid devices. In the presence of nano-clay the overall solar to electric conversion efficiency was improved due to the increase in E_{oc} and FF. As the clay is large enough and does not penetrate in the mesoporous film, the origin of these changes is associated with the variation of the dissolved species in the electrolyte. With the aid of impedance spectroscopy, we have evaluated the influence of CB shifts and recombination rate changes in the photovoltage. The data indicates that the variation of the concentration of Li^+ and I^- in the presence of nano-clay have a direct role in the photovoltage. On the one hand, the drop of dissolved lithium upon nano-clay addition induces an upshift of the TiO_2 CB. On the other hand, the lower amount of iodine activates the indirect recombination path through the dye molecules. These results highlight the potentiality of synthetic nano-clay based electrolytes in the development of stable and high efficiency solar cells and situates the impedance spectroscopy as a robust method for the analysis of DSCs.

Acknowledgements

We acknowledge financial support from Generalitat Valenciana under Project PROMETEO/2009/058. V.G.-P. acknowledge the financial support of Japan Society for the Promotion of Science (JSPS) through its Post-doctoral fellowship for overseas researchers.

Appendix A. Supplementary data

Supplementary data associated with this article can be found, in the online version, at <http://dx.doi.org/10.1016/j.electacta.2016.03.026>.

References

- [1] B. Oregan, M. Grätzel, A low-cost, high-efficiency solar-cell based on dye-sensitized colloidal TiO_2 films, *Nature* 353 (1991) 737–740.
- [2] Q. Yu, Y. Wang, Z. Yi, N. Zu, J. Zhang, M. Zhang, P. Wang, High-Efficiency Dye-Sensitized Solar Cells: The Influence of Lithium Ions on Exciton Dissociation, Charge Recombination, and Surface States, *ACS Nano* 4 (2010) 6032–6038.
- [3] A. Yella, H.W. Lee, H.N. Tsao, C.Y. Yi, A.K. Chandiran, Porphyrin-sensitized solar cells with cobalt (II/III)-based redox electrolyte exceed 12 percent efficiency (vol 334 pg 629, 2011), *Science* 334 (2011) 1203.
- [4] K.L. Li, S. Adams, Optimization of CuSCN Solution Casting for High Stability All-Solid-State Dye-Sensitized Solar Cells, *Nanosci. Nanotechnol. Lett.* 4 (2012) 750–755.
- [5] G.R.R.A. Kumara, A. Konno, G.K.R. Senadeera, P.V.V. Jayaweera, D.B.R.A. De Silva, K. Tennakone, Dye-sensitized solar cell with the hole collector p-CuSCN deposited from a solution in n-propyl sulphide, *Solar Energy Materials and Solar Cells* 69 (2001) 195–199.
- [6] Q.B. Meng, K. Takahashi, X.T. Zhang, I. Sutanto, T.N. Rao, O. Sato, A. Fujishima, H. Watanabe, T. Nakamori, M. Urugami, Fabrication of an Efficient Solid-State Dye-Sensitized Solar Cell, *Langmuir* 19 (2003) 3572–3574.
- [7] U. Bach, D. Lupo, P. Comte, J.E. Moser, F. Weissörtel, J. Salbeck, H. Spreitzer, M. Grätzel, Solid-state dye-sensitized mesoporous TiO_2 solar cells with high photon-to-electron conversion efficiencies, *Nature* 395 (1998) 583–585.
- [8] H. Wang, G. Liu, X. Li, P. Xiang, Z. Ku, Y. Rong, M. Xu, L. Liu, M. Hu, Y. Yang, H. Han, Highly efficient poly(3-hexylthiophene) based monolithic dye-sensitized solar cells with carbon counter electrode, *Energy & Environmental Science* 4 (2011) 2025–2029.
- [9] L. Yang, B. Xu, D. Bi, H. Tian, G. Boschloo, L. Sun, A. Hagfeldt, E.M.J. Johansson, Initial Light Soaking Treatment Enables Hole Transport Material to Outperform Spiro-OMeTAD in Solid-State Dye-Sensitized Solar Cells, *Journal of the American Chemical Society* 135 (2013) 7378–7385.
- [10] X. Huang, Y. Liu, J. Deng, B. Yi, X. Yu, P. Shen, S. Tan, A novel polymer gel electrolyte based on cyanoethylated cellulose for dye-sensitized solar cells, *Electrochimica Acta* 80 (2012) 219–226.
- [11] Q. Li, J. Wu, Z. Tang, Y. Xiao, M. Huang, J. Lin, Application of poly(acrylic acid-gelatin)/polypyrrole gel electrolyte in flexible quasi-solid-state dye-sensitized solar cell, *Electrochimica Acta* 55 (2010) 2777–2781.
- [12] D. Li, D. Qin, M. Deng, Y. Luo, Q. Meng, Optimization the solid-state electrolytes for dye-sensitized solar cells, *Energy & Environmental Science* 2 (2009) 283–291.
- [13] H. Chae, D. Song, Y.-G. Lee, T. Son, W. Cho, Y.B. Pyun, T.-Y. Kim, J.H. Lee, F. Fabregat-Santiago, J. Bisquert, Y.S. Kang, Chemical Effects of Tin Oxide

- Nanoparticles in Polymer Electrolytes-Based Dye-Sensitized Solar Cells, *The Journal of Physical Chemistry C* 118 (2014) 16510–16517.
- [14] P. Wang, S.M. Zakeeruddin, J.E. Moser, M.K. Nazeeruddin, T. Sekiguchi, M. Grätzel, A stable quasi-solid-state dye-sensitized solar cell with an amphiphilic ruthenium sensitizer and polymer gel electrolyte, *Nat Mater* 2 (2003) 402–407.
- [15] W. Kubo, T. Kitamura, K. Hanabusa, Y. Wada, S. Yanagida, Quasi-solid-state dye-sensitized solar cells using room temperature molten salts and a low molecular weight gelator, *Chemical Communications* (2002) 374–375.
- [16] C.-L. Chen, H. Teng, Y.-L. Lee, In Situ Gelation of Electrolytes for Highly Efficient Gel-State Dye-Sensitized Solar Cells, *Advanced Materials* 23 (2011) 4199–.
- [17] L.-Y. Chang, C.-P. Lee, R. Vittal, J.-J. Lin, K.-C. Ho, Enhanced performance of a dye-sensitized solar cell with an amphiphilic polymer-gelled ionic liquid electrolyte, *Journal of Materials Chemistry A* 1 (2013) 3055–3060.
- [18] P. Wang, S.M. Zakeeruddin, J.E. Moser, M. Grätzel, A new ionic liquid electrolyte enhances the conversion efficiency of dye-sensitized solar cells, *Journal of Physical Chemistry B* 107 (2003) 13280–13285.
- [19] P. Wang, S.M. Zakeeruddin, P. Comte, I. Exnar, M. Grätzel, Gelation of Ionic Liquid-Based Electrolytes with Silica Nanoparticles for Quasi-Solid-State Dye-Sensitized Solar Cells, *Journal of the American Chemical Society* 125 (2003) 1166–1167.
- [20] H. Yang, Y.F. Cheng, Z.G. Zhou, Z.G. Chen, F.Y. Li, T. Yi, C.H. Huang, Ionic liquid based electrolyte with mesoporous silica SBA-15 as framework for quasi-solid-state dye-sensitized solar cells, *Chinese Journal of Chemistry* 24 (2006) 1737–1740.
- [21] H. Usui, H. Matsui, N. Tanabe, S. Yanagida, Improved dye-sensitized solar cells using ionic nanocomposite gel electrolytes, *Journal of Photochemistry and Photobiology A: Chemistry* 164 (2004) 97–101.
- [22] T. Kato, S. Hayase, Quasi-Solid Dye Sensitized Solar Cell with Straight Ion Paths: Proposal of Hybrid Electrolytes for Ionic Liquid-Type Electrolytes, *Journal of The Electrochemical Society* 154 (2007) B117–B121.
- [23] J.H. Park, B.-W. Kim, J.H. Moon, Dual Functions of Clay Nanoparticles with High Aspect Ratio in Dye-Sensitized Solar Cells, *Electrochemical and Solid-State Letters* 11 (2008) B171–B173.
- [24] X. Wang, S.A. Kulkarni, B.I. Ito, S.K. Batabyal, K. Nonomura, C.C. Wong, M. Grätzel, S.G. Mhaisalkar, S. Uchida, Nanoclay Gelation Approach toward Improved Dye-Sensitized Solar Cell Efficiencies: An Investigation of Charge Transport and Shift in the TiO₂ Conduction Band, *ACS Applied Materials & Interfaces* 5 (2012) 444–450.
- [25] C. Bisio, G. Gatti, E. Boccaleri, L. Marchese, G.B. Superti, H.O. Pastore, M. Thommes, Understanding physico-chemical properties of saponite synthetic clays, *Microporous and Mesoporous Materials* 107 (2008) 90–101.
- [26] C.-W. Tu, K.-Y. Liu, A.-T. Chien, M.-H. Yen, T.H. Weng, K.-C. Ho, K.-F. Lin, Enhancement of photocurrent of polymer-gelled dye-sensitized solar cell by incorporation of exfoliated montmorillonite nanoplatelets, *Journal of Polymer Science Part A: Polymer Chemistry* 46 (2008) 47–53.
- [27] X. Wang, R. Deng, S.A. Kulkarni, X. Wang, S.S. Pramana, C.C. Wong, M. Grätzel, S. Uchida, S.G. Mhaisalkar, Investigation of the role of anions in hydrotalcite for quasi-solid state dye-sensitized solar cells application, *Journal of Materials Chemistry A* 1 (2013) 4345–4351.
- [28] D. Costenaro, C. Bisio, F. Carniato, G. Gatti, F. Oswald, T.B. Meyer, L. Marchese, Size effect of synthetic saponite-clay in quasi-solid electrolyte for dye-sensitized solar cells, *Solar Energy Materials and Solar Cells* 117 (2013) 9–14.
- [29] Y. Furukawa, K. Tadanaga, A. Hayashi, M. Tatsumisago, Evaluation of ionic conductivity for Mg-Al layered double hydroxide intercalated with inorganic solid, *Solid State Ionics* 192 (2011) 185–187.
- [30] Z. Zhang, C. Xu, F. Qiu, X. Mei, B. Lan, S. Zhang, Study on fire-retardant nanocrystalline Mg-Al layered double hydroxides synthesized by microwave-crystallization method, *Sc. China Ser. B-Chem.* 47 (2004) 488–498.
- [31] A. Hauch, A. Georg, Diffusion in the electrolyte and charge-transfer reaction at the platinum electrode in dye-sensitized solar cells, *Electrochimica Acta* 46 (2001) 3457–3466.
- [32] F. Fabregat-Santiago, G. Garcia-Belmonte, I. Mora-Sero, J. Bisquert, Characterization of nanostructured hybrid and organic solar cells by impedance spectroscopy, *Physical Chemistry Chemical Physics* 13 (2011) 9083–9118.
- [33] V. González-Pedro, X. Xu, I. Mora-Seró, J. Bisquert, Modeling High-Efficiency Quantum Dot Sensitized Solar Cells, *ACS Nano* 4 (2010) 5783–5790.
- [34] F. Fabregat-Santiago, J. Bisquert, L. Cevey, P. Chen, M. Wang, S.M. Zakeeruddin, M. Grätzel, Electron Transport and Recombination in Solid-State Dye Solar Cell with Spiro-OMeTAD as Hole Conductor, *Journal of the American Chemical Society* 131 (2009) 558–562.
- [35] S.R. Raga, E.M. Barea, F. Fabregat-Santiago, Analysis of the Origin of Open Circuit Voltage in Dye Solar Cells, *The Journal of Physical Chemistry Letters* 3 (2012) 1629–1634.
- [36] F. Gonell, M. Haro, R.S. Sánchez, P. Negro, I. Mora-Seró, J. Bisquert, B. Julián-López, S. Gimenez, Photon Up-Conversion with Lanthanide-Doped Oxide Particles for Solar H₂ Generation, *The Journal of Physical Chemistry C* 118 (2014) 11279–11284.
- [37] A.Y. Anderson, P.R.F. Barnes, J.R. Durrant, B.C. O'Regan, Quantifying Regeneration in Dye-Sensitized Solar Cells, *The Journal of Physical Chemistry C* 115 (2011) 2439–2447.